Microstructural design of printed graphite electrodes for lithium-ion batteries

Gastol, Dominika; Capener, Matthew; Reynolds, Carl; Constable, Christopher; Kendrick, Emma

DOI:
10.1016/j.matdes.2021.109720

Document Version
Publisher's PDF, also known as Version of record

Citation for published version (Harvard):
Gastol, D, Capener, M, Reynolds, C, Constable, C & Kendrick, E 2021, 'Microstructural design of printed graphite electrodes for lithium-ion batteries', *Materials and Design*, vol. 205, 109720. https://doi.org/10.1016/j.matdes.2021.109720

Materials & Design 205 (2021) 109720

Contents lists available at ScienceDirect

Materials & Design

journal homepage: www.elsevier.com/locate/matdes

Microstructural design of printed graphite electrodes for lithium-ion batteries

Dominika Gastol [a], Matthew Capener [b], Carl Reynolds [a], Christopher Constable [b], Emma Kendrick [a,*]

[a] School of Metallurgy and Materials, University of Birmingham, Birmingham B15 2TT, UK
[b] WMG, University of Warwick, Coventry CV4 7AL, UK

ARTICLE INFO

Article history:
Received 22 December 2020
Revised 1 April 2021
Accepted 7 April 2021
Available online 9 April 2021

Keywords:
Lithium-ion
Graphite
Electrode
Tortuosity
Additive manufacturing

ABSTRACT

Performance properties of lithium-ion battery electrodes; capacity, rate and lifetime, are determined by the design of the coating composite microstructure. The internal pore structure and electronic networks for high coat weight graphite electrodes are manipulated through changes in the ink rheological properties, and through an syringe dispensing printing process. The rheological properties of a water-based, high viscosity graphite ink were optimised using a secondary solvent for the rheological requirements of a syringe dispensing method. The microstructure of high coat-weight battery electrodes produced from printing and tape cast methods were compared and the electrochemical performance evaluated. Cross sectional analysis of the slurry cast coatings showed improved component homogeneity, lower graphite alignment with 0.1% to 10% weight increase of the secondary solvent, with a corresponding change in tortuosity of the electrodes of 5.3–2.8. Improved cycle life is observed with a printed electrode containing an embedded electrolyte channel. Performance properties were elucidated through charge discharge, GITT and PEIS measurements. Improved electronic conductivities, exchange currents and diffusion coefficients were observed for the syringe deposited electrode. This digital deposition process for manufacturing electrodes shows promise for further optimisation of electrodes for long-life, high energy density batteries.

1. Introduction

Lithium ion batteries (LIB) must overcome two key technical challenges to meet the demand for high throughput production of EVs; further reduction of the production costs and an increase in energy density of the battery pack [1]. While the cost of production per kWh has decreased significantly from 1.183 US$ in 2010 to 153 US$ in 2019, the target of 100 US$/ kWh, a cost parity to their internal combustion engine counterparts, has still not been reached [2]. Three key fields have been highlighted for further cost reduction in battery manufacturing; a) quality control, in order to minimise the scrap generation in cell production [3]; b) innovation in electrode manufacturing to increase the energy density and production yields, through design of the coating processes [4–6]; c) development of high energy density materials and their optimisation [7]. Much of the current research is focused on new materials and chemistries for improvement of the current and next generation Li-ion batteries. Silicon-dominant anodes and nickel-rich cathodes are being implemented to increase the energy density of the Li-ion battery, however further progress is needed to extend their lifetime performance [8,9]. To further improve energy density, other new materials which undergo electrochemical conversion rather than intercalation mechanism are also being investigated [10]. Li-S, Li-O_2 and Li-CO_2 demonstrate a significant gravimetric energy density enhancement compared to Li-ion systems. However, their performance is hampered by poor cycle life performance and efficiency (resulting from electrode volume expansion for Li-S and high over potentials), chemical instability of electrolytes/ electrodes and transport limitations of electron and lithium ions [11–13].

Conventionally, battery electrodes are prepared from a slurry consisting of dispersed electrochemically active material, conductive additives, binder and a suitable solvent that dissolves the binder [14]. The composite based slurry is typically coated by tape casting methods onto the current collectors (copper for anodes and aluminium for cathodes), and subsequently dried to form the battery electrodes. For both intercalation and conversion materials, design of electrode structures is also key for optimisation of performance properties. Electrodes must be designed with optimum porosity, pore structure, carbon and active materials distribution, to control and optimised the electronic and ionic transport within the electrodes. This careful micro and macro-structure multi-component

* Corresponding author.
E-mail address: e.kendrick@bham.ac.uk (E. Kendrick).

https://doi.org/10.1016/j.matdes.2021.109720
0264-1275/

composite design is required to control the volume expansion, morphological changes and hence the effective 3D electronic and ionic diffusion through the electrode, at all states of charge. New cell geometries, electrode architectures and fabrication methods can offer solutions to some of the lifetime and cost challenges for LIB [1,7,15]. Further advances will only be realised by changes to the current manufacturing technologies for the control and design of new electrode architectures. Initial investigations into alternative coating techniques such as; flexible suspension atomisation with spray deposition, electrode sintering or 3D printing, show improvements in performance through greater control in the microstructure of the electrodes [1,14,16–19].

An effective method of achieving high energy batteries, is to increase the areal capacity of the battery electrodes, and create higher loading and thick electrodes (currently electrodes are manufactured with thicknesses of 50 – 100 μm), in order to minimise the relative weight and volume of inactive components, i.e. separators and current collectors [1,20]. This introduces challenges related to lithium-ion transport pathways and uniform electronic conductivity, both of which are critical to energy and power output. Transport limitations are associated with poor electrode wetting, tortuous and long lithium-ion diffusion and electronic paths, as well as high impedance occurring due to the point contacts between individual particles [1,3,4]. Several design aspects for the electrodes have been investigated to optimise the electronic and ionic transport within the cells [21,22]. Smaller particle sizes of the active material can reduce polarisation due to the increased surface area for reaction and to decrease capacity loss at high discharge rates by minimising the Li-ion diffusion path between the particles [23,24]. Freeze-drying to prepare electrodes has also shown promise in improving wettability, better rate performance and capacity retention potential due to the lower touristy structure arising from the alignment of graphite flakes out-of-plane [25]. At an electrode level, to overcome some of these transport limitations different structural designs such as; graded porosity and hierarchical architectures in combination with new electrode deposition techniques have shown promise in overcoming some of the challenges for high coat-weight electrodes [5,8,9,16,21]. For slurry cast electrodes, the rheological properties of the slurries and inks are extremely important for realising homogeneous, thick, porous and electronically conducting films. These rheological properties of the electrode slurry are governed by the volume fraction of solids, particle shape and surface tension of the incorporated materials [14,26]. The dispensing fluid needs to have shear thinning properties, to flow and form a homogenous coating. The thixotropic behaviour is also important to prevent sagging and pattern definition loss. Highly thixotropic fluids are often obtained through high solid content slurries, however, an increase content of the active material can lead to increased shear thickening behaviour of the slurry and consequently, blockage of the dispensing nozzle. An alternative approach that avoids increasing solid content, is to alter the viscosity through the introduction of a small amount of an immiscible secondary fluid that creates capillary bridges between the particles to form a network [27–29], There are two states of capillary suspension that can be differentiated depending on the three-phase wetting angle (Q_{3p}) that is created by the secondary liquid and the solid phase. When the particles are wetted by the incorporated minority liquid ($Q_{3p} < 90°$) - the pendular bridges are created between the particles. However, when a dominating fluid exhibits better wetting properties than the secondary fluid ($Q_{3p} > 90°$), the capillary state is formed and the particles form clusters around small volumes of the immiscible liquid [26,29–32].

In this work, the rheological properties of the inks are modified and a novel dispensing printing method utilised to produce thick electrode coatings (Fig. 1) [33]. Contrary to the conventional blade coating method, the printing dispenser offers precision deposition of the slurry, the accuracy of which is controlled by the flow properties of the inks and size of the dispensing nozzle. To implement thick, or high coat weight, electrodes with this dispensing syringe technology, the flow properties of the ink require optimisation with a particle size 10 times smaller than the nozzle diameter to prevent clogging [34]. The deposition and electrochemical performance of a small particle size graphite (KS6) was investigated as a model system. Capillary suspension slurries were designed to transfer the formulations and mixes used in draw-down coatings to this dispensing printing method. KS6 is not a typical active material graphite used in battery electrodes due to its small particle size and high surface area and is usually used as an additive. However, the natural flake graphite offers interesting control options for graphite flake alignment in an electrode and can be utilised to design lower tortuosity pore networks for ion transport. In the 'standard' electrode slurries with typical high solid loadings and large particles sizes blocking of the syringe nozzles occurred during deposition. Typically, higher solid contents are required for high coat weight electrodes from tape casting methods, as this improves adhesion and conductivity properties. In this work lower solid contents were used (20%) which were subsequently deposited onto current collectors by both tape casting and extrusion deposition methods for comparison. By optimising the rheological properties of the ink, improving the dispersion properties, and changing the thixotropy it was possible from the extensive shear thinning to extrude the slurries through the nozzle with no blocking, and produce stable semi-solid structures after deposition for maintaining the deposited structured electrode. In this work, the rheological properties of the inks were modified by incorporation of different percentages of 1-octanol as a secondary solvent in a water-based slurry. The effect upon the electrode microstructures from the rheological changes, and the deposition method were analysed, and their electrochemical parameters elucidated.

2. Experimental

2.1. Slurry preparation and rheology

The same slurry preparation method was used for both printing methods. Composite water-based inks were made with 90 %w/w active component, (Graphite KS6L, Imerys), 5%w/w conductive carbon (Timcal C65, Imerys) with binders 2%w/w CMC (Bondwell BVH8, Ashland) and 3% w/w SBR (BM-451B Zeon). The flaked graphite KS6L was selected as an active material of D90 equal to 6.5 μm (Fig. S1). Crack creation in a colloidal suspension, depends on a particle radius r and the particle shear modulus G. To increase the critical cracking thickness ($CCT = h_{max}$), the particle volume fraction and size was adjusted with additional solvent [35,36]. The solid content of the inks was adjusted to 20 wt% with an addition of DI water and 1-octanol to the mixture in ratios ranging from 100, 99.5:0.5, 99:1, 95:5 and 90:10. The anode slurries were prepared with the use of a Thinky ARE 250 centrifugal mixer (Thinky, USA). The rheological behaviour of the prepared anode slurries was investigated with the use of a rotational Rheometer, (RheolabQC, Anton Paar). The viscosity measurement of the inks was conducted at 25 °C using a concentric cylinder measuring system, comprising of: disposable measuring cylinder B-CC27 and C-CC27 cup for the low viscosity slurries (0% and 0.1% octanol). Single-use measuring cylinder B-CC14 and cup C-CC14 and a cup holder (MAT: 79019) was utilised for the inks exhibiting paste-like properties: 0.5 wt%, 1.0 wt%, 5.0 wt%, and 10.0 wt% (Table S2). Three interval thixotropy test (3ITT) measurements were performed by applying a shear rate of 1 s^{-1}, 1000 s^{-1} and 1 s^{-1} sequentially in three intervals of 100 s.

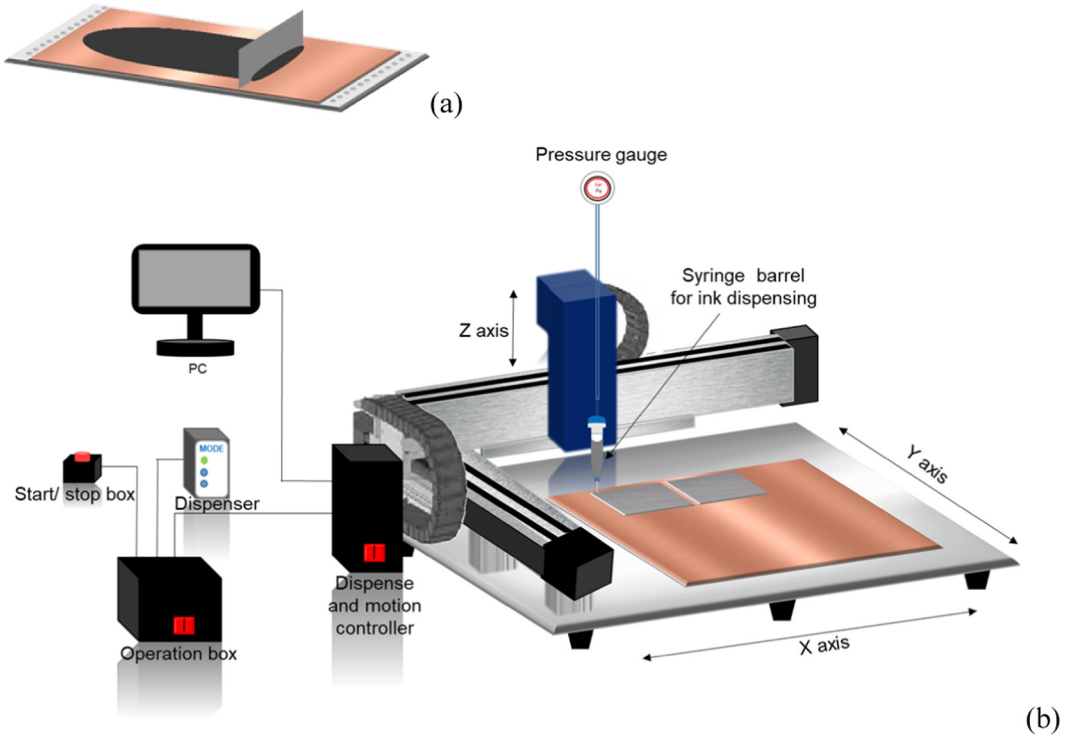

Fig. 1. Schematic of coating methods (a) Dr Blade used as a conventional coating method in a laboratory set-up, and (b) the automated dispensing system utilised for digital deposition of electrodes (B), pictures not-to-scale.

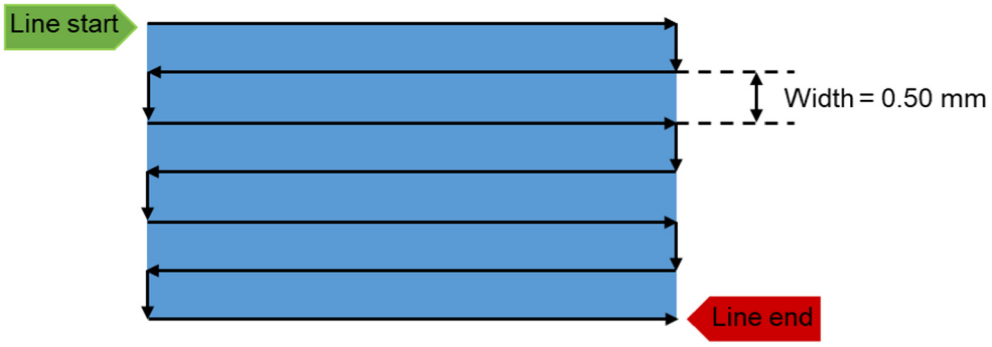

Fig. 2. Illustration of the rectangle S path command applied for the digital electrode printing with the filled area of 40 cm2.

2.2. Coating parameters

The prepared slurries were coated onto the copper foil (10.2 μm) using a draw-down coater (K Paint Applicator, RK Print-coat Instruments, UK) with a micrometre adjustable doctor blade. The inks were applied to the foil before coating using a 10 mL syringe in order to maintain consistency of the coating process. The prepared coatings were dried on a hot plate at 50 °C and then transferred to the vacuum oven and dried at the same temperature for ca. 48 h to ensure minimising of any water prior to the cell construction.

The Automated Dispensing System, designed and manufactured by KWSP, was employed for a deposition of the electrodes. The digital printing set up comprised of: the DispenseMotion™ controller, the robot, and the dispensing system components, (Fig. 1) [37]. A computer software was programmed to dispense the anode ink in a rectangle pattern (S path) to fill area of 40 cm^2 on a copper current collector, Fig. 2. The gantry robot, controlled in X, Y, and Z coordinates executed the computer program, where the slurry was deposited in a non-contact mode through a stainless-steel needle with a diameter of 0.250 mm attached to a dispensing nozzle, the height of which above the copper substrate was set using feeler gauges. The printing was performed at a speed of 100 $mm{\cdot}s^{-1}$, line width 0.50 mm and the pressure adjusted to 40 psi. The dispensing printer was employed for a deposition of the ink that was established to possess the best results in regard to the obtained structure of the coating and viscosity that enables controlled deposition of the ink for high precision printing of the patterned electrodes.

The ink containing addition of 1.0 wt% 1-octanol, was utilised for digital deposition of the anodes.

2.3. Cross- section and SEM analysis of coatings

The microstructure of the anode distribution of the active material and carbon black was investigated by conducting SEM analysis of the cross- sectioned coatings prepared with different 1-octanol content. The cross- sections were performed with an application

of Hitachi Ion Milling System (IM4000 plus) at an acceleration voltage of 5 kV for 3 h. SEM analyses were conducted on pristine (non-cycled) materials and the cross-sectioned coatings using a Carl Zeiss Sigma Field Emission Scanning Electron Microscope under an acceleration voltage of 10 kV and with an in-lens detector. For the SEM images, a magnification of 2000 × was utilised for investigation of the active material particle orientation. Firstly, a threshold was performed in order to generate a black and white micrograph with the white phase corresponding to the graphite particles. Subsequently, the Image J directionality plugin with a Fourier components function was employed and the black and white images were generated, see Table S1, where the black phase was assigned to the graphite particles. The level of alignment was assessed from histograms of the particle's alignment from 0° to 90°, where 0° indicated parallel position to the current collector, and 90° shows perpendicular alignment of the active material.

The electrode density was obtained by measuring the weight (g) and thickness (l) of the electrode. The area of the electrode (A) was 1.767 cm^2. The electrode density was determined from the Eq. (1).

$$\rho_{AM} = \frac{g}{A \cdot l} \tag{1}$$

$$\Phi = 1 - \frac{\rho_{AM}}{\rho} \tag{2}$$

The porosity of the electrode was calculated according to the formula (2), where ρ_{AM} means density of the active mass and ρ refers to the theoretical density of all the components in the electrode. The thickness was measured with a micrometre gauge.

2.4. Electrochemical testing of the coating in the half-cells

The printed anodes were tested electrochemically in the coin cells half-cells. The coat-weight of the electrodes was adjusted by changing the doctor blade gap to achieve areal capacity of approx. 3.1 mA.h cm^{-2}. Dried coatings were processed in a dry room with a dew point of −45 °C. 2032 coin cells were constructed with electrode discs (15.0 mm in diameter), tri-layer 2025 separator (Celgard) and lithium metal foil counter electrodes (15.6 mm in diameter, 0.25 mm thickness, PI-Kem) and 60 μL of 1 mol/L $LiPF_6$ in EC: DMC 1: 1 electrolyte and sealed with a hydraulic crimper (MSK-110, MTI Corporation, USA).

Electrochemical testing was performed on a Biologic BCS 805 series cycler. **Initial capacities and formation** were obtained by applying the following protocol: Rest for 12 h to enable wetting, constant current lithiation at 0.05C to 5 mV vs Li/Li+ and delithiation to 1.5 V vs Li/Li+ at the same rate using constant current (CC) step repeated twice. Followed by 0.2C discharge and charge steps with the same voltage limits as mentioned before and the rest interval between the steps. The **cycle life** testing was performed as CC charge at 0.2C and discharge at 0.5 C for 50 cycles. **Potentiostatic electrochemical impedance spectroscopy** (PEIS) was conducted after formation step and after cycle life testing, at the frequency range from 10 mHz to 500 kHz, with a 10-mV perturbation voltage, at 1.5 V vs Li/Li^+. The experimental data obtained from the PEIS scans were fitted and the resistances extracted from the different frequency components, using the equivalent circuit model presented in Fig. 3 [15,38–40]. The equivalent circuit model was built around the observed impedance for each cell. The **formed cells** were fitted with a series resistance (R_s, contact resistance and capacitance (R_2, C_2) at high frequencies, and a Constant Phase Element (*CPE, Q*) and resistance at medium frequencies. A low frequency region occurred below 17.5 Hz for all formed electrodes. This low frequency region could be fitted with a CPE and a resistor with a diffusion related tail observed at the ultra-low frequencies <1 Hz. The printed and formed electrode exhibited only a diffusion tail at frequencies less than 17.5 Hz. The diffusion tail could be fitted with a modified Warburg coefficient for finite diffusion (M) in both cases. In the **cycled electrodes**, two distinct semi-circles were visible with a diffusion tail. The initial high frequency (> ~1.5 kHz) semi-circle could be fitted with a CPE and resistor and is likely related to the SEI growth upon the electrode, the intermediate frequencies between ~ 3 Hz and 1.5 kHz could be fitted to a Gerisher element (G), and the frequency tail at less than 3 Hz fitted to a diffusion limited modified Warburg element (M) [41].

The low frequency regions correspond to the ionic transport in the solid (graphite), and the high frequency corresponds to the electronic transport, or contact resistances. The intermediate frequencies correspond to the charge transport in porous structures in the Li-ion batteries. This charge transfer in the porous electrode is determined by the ionic resistance R_{ion} inside the electrolyte phase within the pores of the electrode, the charge transfer of lithium across the surface of the graphite $R_{Gr,}$ and the transport of lithium across the R_{SEI}. The characteristic frequency (f_c) or time constant reciprocal (τ_c^{-1}) of the diffusion processes in a finite process can be estimated from the related diffusion length (L_c), (Eq 6). For example, the diffusion coefficient (D_c) of a 1 M $LiPF_6$ electrolyte in EC:DMC is ~ 2 × 10^{-10} m^2s^{-1} [42,43]

$$\frac{1}{\tau_c} = f_c = \frac{D_c}{L_c^2} \tag{6}$$

Assuming finite diffusion, a frequency response for transport of ions in an electrolyte pore of size ~ 1 μm is 200 Hz, and a pore size of 0.1 μm or 10 μm, 20 kHz or 2 Hz respectively. In the case for these systems, the resistivity from the electrolyte in the pore, R_{pore}, contributes to the impedance observed below ~20 Hz, which are similar frequencies to those observed for the charge transfer resistance across the graphite interface, R_{Gr} and across the solid electrolyte interface (SEI) R_{SEI}. For the formed cells, there is also a resistive contribution to the frequencies lower than 10 Hz, which is likely to be electrolyte transport in larger pores contained within the electrode in addition to diffusion within the graphite particles. More elucidation of the contributions to the impedance from the ion transport in the pore network can be obtained by symmetrical cell tests but has not been done as part of this work. The values of conductivity (σ) and exchange current density (j_0) can be determined based on the following Eqs. (7) and (8).

$$\sigma = \frac{1}{R_{ct}} \cdot \frac{t}{A} \tag{7}$$

$$j_0 = \frac{RT}{R_{ct} F S_{eff}} \tag{8}$$

where t refers to the thickness and A the area of the electrode and S_{eff} is the effective electrode surface area for lithiation (8) applied to calculate the current exchange density. R is Boltzmann constant T is temperature, F is Faraday's constant.

$$S_{eff} = nS_{particle} = \frac{\varepsilon_{act} \cdot V_{electrode}}{V_{particle}} S_{particle} \tag{9}$$

S_{eff} is the effective surface area in the electrode and is used to calculate the electrode–electrolyte surface area for ionic transport across the graphite interface. $S_{particle}$ is the surface area relating to the particle size, which is estimated as the surface area of a sphere ($4/3\pi r^2$) with radius being half the average particle size; r = 3.25 μm [35]. The effective surface area for lithium exchange should be similar for each electrode as each coating mass loading is the same. This calculation therefore gives a good comparison between electrodes. It is not possible to estimate the electrochemically active specific area (EASA) from the edge sites of the flaked graphite as we do not know the ratio of the basal plane to the edge.

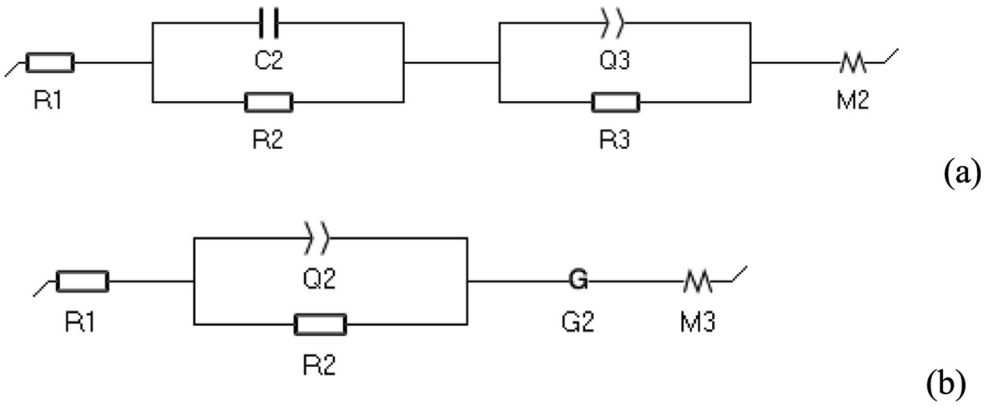

Fig. 3. Electric circuit diagrams used to fit the EIS data: before (a) and after (b) cycle life testing, where R is a resistor, C is capacitor, Q is a Constant Phase Element, G is a Gerisher element, and M is a modified Warburg coefficient for finite diffusion.

The tortuosity was elucidated from the binary images (Table S1), using *TauFactor* [44] under the standard settings, assuming the black phase as the diffusing phase. Binary images were based on image segmentation which matched the black porous phase fraction with the calculated porosity value (see Table S3). The "*flow through*" type tortuosity calculated here ignores the good contribution of dead-end pores. An analysis using a frequency domain approach, for example as set out by Landesfeind *et al.* [45] is recommended for further investigation. The McMullin number (N_M) can be calculated from the ratio of the tortuosity (τ_u) and porosity (ε_p) (Eq. (10))

$$N_M = \frac{\tau_u}{\varepsilon_p} = \frac{R_{ion} \cdot A \cdot \kappa}{t} \tag{10}$$

Rate testing was not reported here due to difficulties in obtaining reproducible capacities using the constant current discharge method. Dendritic lithium formed on the thick electrodes very quickly during the testing protocols which resulted in short circuit of cell. Full cell testing would be preferable to overcome the ½ cell limitations, using constant current and constant voltage lithiation of the graphite, however this is not the subject of the current study.

Galvanostatic intermittent titration (GITT) was performed on the selected electrodes from the drawdown coating: with no addition of the fatty alcohol and with 1.0 wt% 1-octanol content, compared with the printed electrodes modified with the same concentration of the secondary fluid. The GITT measurements consisted of a series of current pulses applied at fixed voltages range of 0.1 to 1.5 V, each followed by a relaxation period. The testing was performed by applying a C/10 current transient for 2.5 min, followed by a relaxation period to reach an OCV. The diffusion coefficient was calculated using equation 10, where V_M refers to molar volume of active material, M_{AM} is atomic weight of active material, m_{AM} is mass of active material, and τis duration of current pulse (150 s).

$$D_{s=} \frac{4}{\pi\tau} \left(\frac{m_{AM} V_M}{M_{AM} S_{eff}}\right)^2 \left[\frac{\Delta E_s}{\Delta E_t}\right]^2 \tag{10}$$

3. Results and discussion

3.1. Doctor blade coatings and ink optimisation

Prior to the application of the digital deposition technique, the investigated slurries were coated with the doctor blade and their viscosity properties were studied. The addition of secondary fluid had a notable effect on the rheological properties of the anode slurries. Shear thinning is observed in all cases. The viscosity of the inks in the low shear rate region increased by two orders of magnitude on increasing the weight fraction of secondary fluid from 0.1 to 0.5 wt%. The observed shear-thinning behaviour can be attributed to the capillary forces of water and 1-octanol on the solid particles, which formed the sample spanning networks [29,30], as well as alignment of the agglomerates [46]. Further increases in the octanol weight fraction have no significant effect on the magnitude of the viscosity, as a stable capillary network is formed. However, a small area of shear thickening can be noted around 10 s^{-1} for the slurries1.0 and 5.0 wt% of 1-octanol.

It can be seen from Fig. 4 that formation of the capillary suspensions affects not only the low shear properties of the inks, but also viscosity at high shear rate. This indicates capillary networks do not break down when the high shear forces are applied. Therefore, the properties of the ink are not affected with the application of high-speed deposition technique.

The change in rheology on addition is typical of a pendular fluid i.e. [47]. Addition of a secondary fluid causes an initial steep increase in viscosity, at low amounts of secondary fluid, due to formation of binary capillary bridges between particles (or agglomerates). A maximum is observed where the capillary bridges begin to coalesce and the aggregates start to form as shown in Fig. 5, this aggregation is known as the furnicular state. The precise ratio of secondary fluid to solid that induces this transition depend on the coordination number and contact angle of the secondary fluid on the particles, we observe the transition at approximately 0.035. Above this ratio, the viscosity of the slurry decreases, due to the formation of larger agglomerates that destabilise the structure. At very high amounts of secondary fluid, phase separation occurs, as seen at 10% 1-octanol. The rheological properties of the inks have a profound effect upon the distribution of carbon black throughout the electrode and the alignment of the graphite particles in the deposited electrode, as shown in Fig. 6. It should be noted that that further optimisations can be performed to further increase the solid content whilst maintaining the good extrusion and ink structure properties but is not the subject of this work.

3.2. Graphite particle directionality analysis, and porosity of the electrodes

Carbon black (CB) agglomerates are visible in the microstructure of the coatings at low levels of octanol addition (0.1 and 0.5, % octanol to DI water content ratio). The increase of octanol content up to 1.0 wt% enhances the CB distribution between the graphite particles, this could be due to the increased viscosity of the inks, and the higher shear forces induced in the mixing process

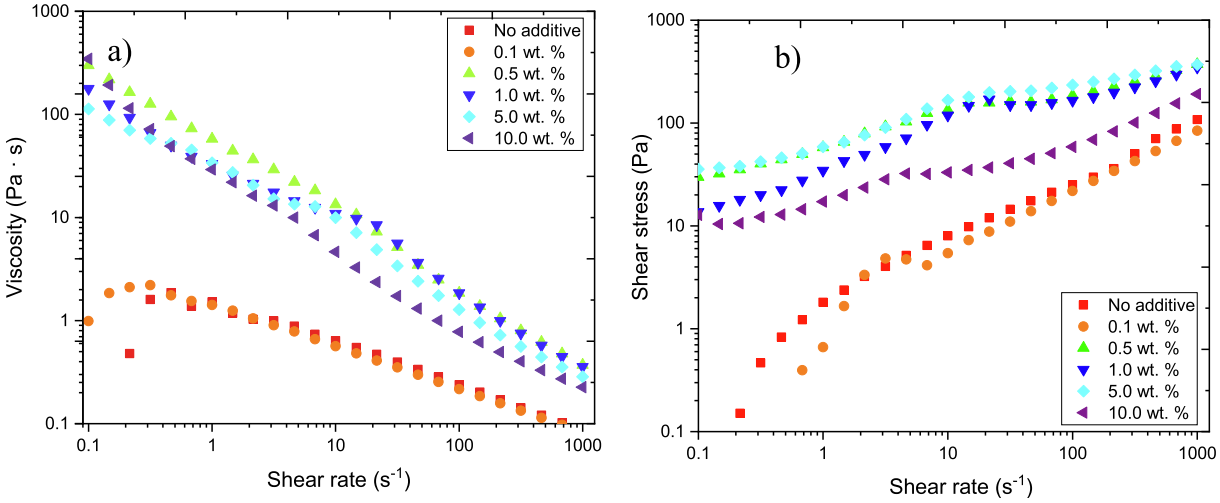

Fig. 4. Flow behaviour curves for the anode inks prepared without and with an addition of 1-octanol at 0.1 wt%, and 0.5 wt%, 1.0 wt%, 5.0 wt%, and 10.0 wt%. (a) Effect of viscosity with shear rate, (b) stress–strain curve.

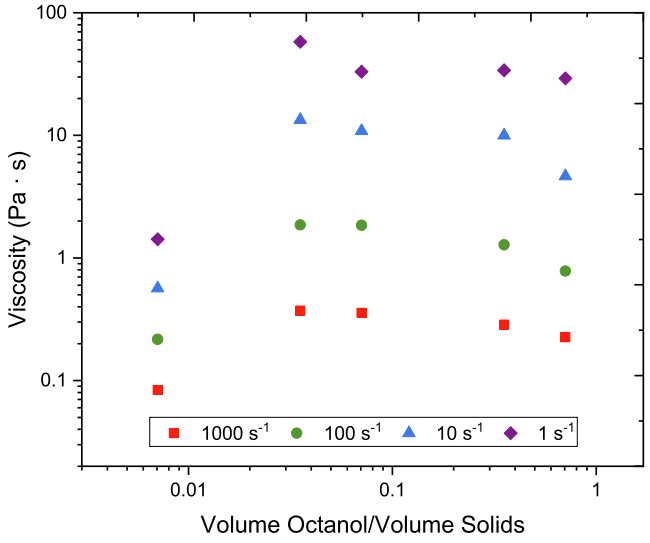

Fig. 5. Viscosity vs. the ratio of 1-octanol and solids volume fractions at different shear rates.

upon the carbon black agglomerates. In addition, there is a change in the alignment of the graphite flakes which contributes to the rise of the porosity of the coating, increasing from 60 to 71%. The formed voids in the structure enhance dispersion of the CB and create the electrical conduction pathways, observed in the coating prepared with 1.0 wt% of 1-octanol. The presence of secondary fluid in the slurry structure enhanced the percolation threshold [48,49]. However, a degradation of the electrode coating structure was observed at 10.0 wt% content of the secondary fluid. As shown in Fig. 4, all the slurries exhibited shear thinning behaviour, however the large physical changes, and agglomerated particles shown in the resulting electrode after drying indicates that at 10% octanol content, the slurry has reached saturation of the immiscible polar liquid and consequently there is a deterioration of the capillary network, which results in the observed structure breakdown in the electrode. From previous work [25] it has been shown that the capillary bridges between particles reduce particle mobility and increase the drying rate of the bulk solvent next to the substrate. As the bridges between particles are filled with the solvent (water) with a higher vapour pressure, the total drying time decreases with increasing amount of secondary fluid. CMC is used as a thickening agent in these water-based systems, it stabilises the slurry from sedimentation and coats the graphite and carbon black in a surface layer which aids the dispersion of the components in the water solvent. The CMC is necessary in these slurries as it coats the graphite surface, and therefore the polar secondary solvent can form stable capillary suspensions with wetting angles <90 °C. The SBR is assumed to be a binding agent and as a rubber it helps to give a degree of flexibility to the thicker coatings, although it also adds significantly to the resistive properties of the coatings. The secondary solvent octanol doesn't dissolve into the water and will form capillary bridges between the graphite particles. With the increase in the secondary solvent, we observe large pore sizes in the cross-sectional SEM, and we see less alignment of the flakes to the current collector. Table 1 shows the calculated density and porosity values of the resulting electrode according to the wt. % concentration of the secondary fluid in the slurry. This can be hypothesised as related to the formation of the capillary networks between particles. If the capillary networks are formed between the edges of the graphite, rather than the basal planes, then the particles will not align parallel to each other, and this relates to the decrease in Q (no. of particles) with alignment of 0° (Fig. 7). For the 10 % octanol, clumps of graphite were observed in agglomerations rather than a complete dispersion of particles. In this case the deposition of the agglomerations and was reflected in the dried electrode and the level of graphite alignment was also reduced.

It can be noted from the density and porosity measurements, that the highest porosity of 70% is exhibited by the coating containing 1.0 wt% of octanol with corresponding the lowest density value of 0.6 g cm^{-3}, also apparent in the SEM micrographs, Fig. 6.

With increasing content of the fatty alcohol, the alignment of the graphite particles changed from parallel to perpendicular to the current collector , as has been reported elsewhere [31]. Fig. 7 shows the differential a) and cumulative distributions b) of the graphite particle orientations relative to the current collector.

Where Q0 is related to the proportion of particles exhibiting a particular orientation, where 0° is aligned to the current collector and 90° is perpendicular to the current collector. It can be observed that the alignment of the active material changes gradually. The highest increase of the perpendicular orientation was noted for electrodes containing 0.5 wt% and 10.0 wt%. Although, it should be also stated that the highest concentration resulted in the microstructure collapse (Fig. 6). The degree of carbon black dispersion and the level of octanol addition are likely to influence the degree of orientation of the graphite and affect the porosity. From

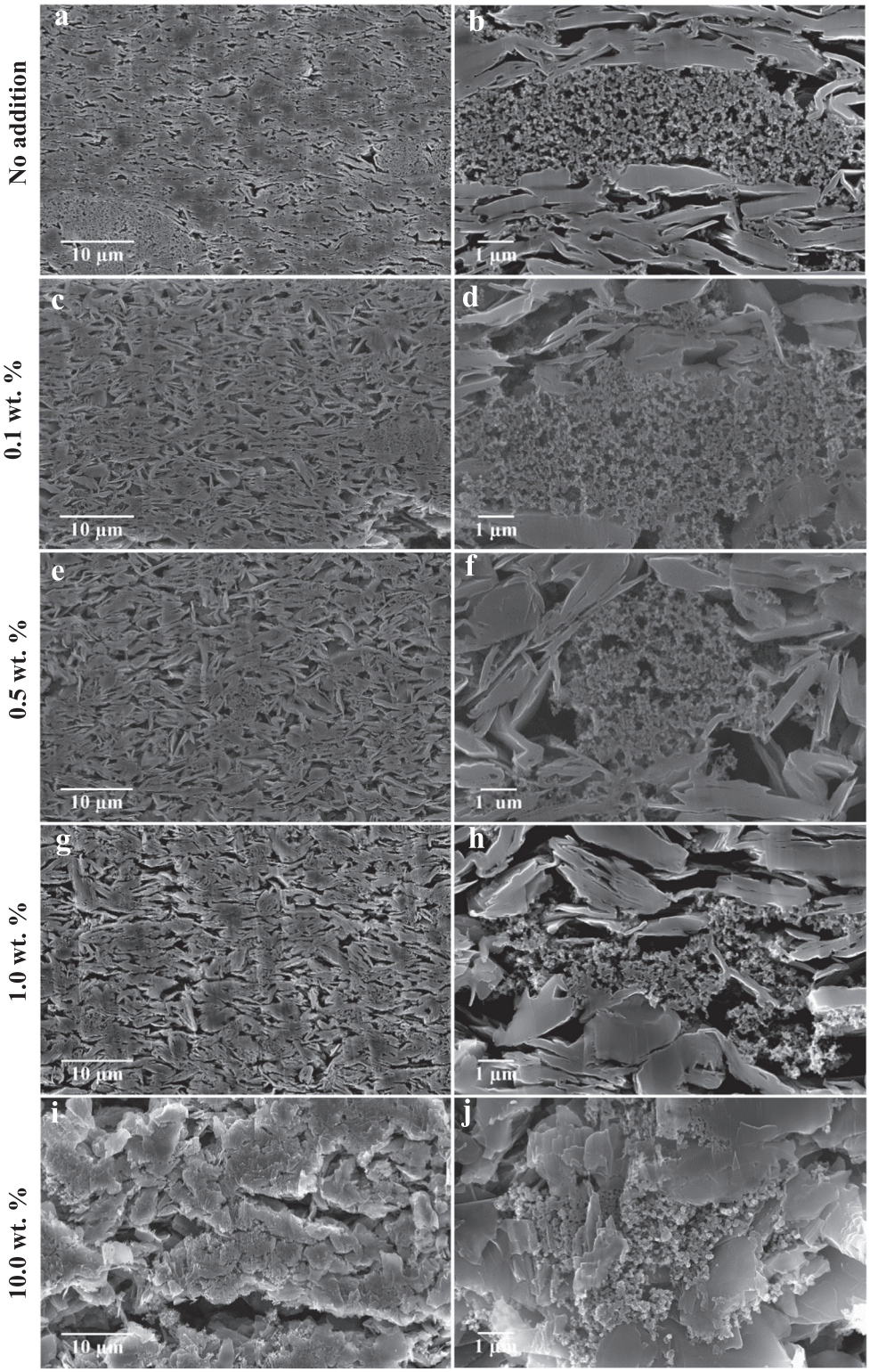

Fig. 6. Cross-sectional SEM micrographs of the anode coatings prepared with different DI water to 1-octanol ratios.

the SEM images (Fig. 6) we can see that the carbon black is not as well dispersed as that for 1% octanol. This is likely why the orientation is more affected at 0.5% octanol, which forms isolate clumps of carbon black surrounded by graphite, compared to the chains of carbon black surrounded by graphite at 1% octanol content.

This initial formation capacities were tested for all of the inks, Fig. 8 illustrates the observed discharge (lithiation) and charge (delithiation) with the first cycle irreversible capacity losses (ICL) of the anode half-cells assembled with electrodes made with different octanol content. It should be noted that ICLs are attributed to the graphite particle size utilised in this study, which has a greater surface area (20 m^2g^{-1}) compared to standard LIB graphite (0.9–4 m^2g^{-1}) and hence increased number of edge sites for electrolyte decomposition [50,51], Table 2. Octanol has a higher boiling point than water (195 °C) but should be removed in the drying process. If there are small traces which remain in the electrode after

Table 1
calculated thickness of the graphite coated film, density and porosity values with increasing wt. % concentration of the secondary fluid in the electrode content, calculated from the measured weight and thickness.

Sample, 1-octanol fraction	Thickness (μm)	Density (g cm^{-3})	Porosity (%)
No additive	120 (5)	0.84 (2)	59.3 (2)
0.1 wt%	113 (4)	0.86 (1)	59.7 (5)
0.5 wt%	140 (9)	0.70 (1)	67.2 (4)
1.0 wt%	158 (7)	0.62 (1)	70.9 (6)
10.0 wt%	157 (9)	0.65 (1)	69.4 (3)

drying, this may be reflected in the slight increase in irreversible capacities with increasing octanol content. In addition, the slight increase in first cycle loss may also be due to greater separation of particles in the mixing process, and hence higher surface area. It is noted, however, that the additional efficiency loss is negligible up to ~ 1% octanol content.

3.3. Digital syringe deposition and ink optimisation

Initial results using the ink with optimised rheology resulted in poor adhesion of the digitally printed electrodes. This was in part due to the requirement for thicker electrodes to maintain a similar coat-weight per unit area to the doctor blade coated electrodes. The SBR binder content was therefore increased slightly to 4.0 wt %, to improve the elasticity and mechanical properties of the coating. The flow initiation and shear stress properties of the optimised ink were compared with a 3.0 wt% SBR content slurry and showed little change in properties (Fig. 9a). In addition to this, the time dependant viscosity recovery of the ink after printing was evaluated by conducting the 3ITT, again showing little rheological different between the two inks, Fig. 9b. As observed the viscosity recovers rapidly after the high shear rate step, and there is no impact observed when increasing the SBR content. Porosity = 72.67 (2) %, density = 0.58 (3) g·cm^{-3}.

Fig. 10 shows a representative pattern obtained from the printing process which has been electrochemically tested. The printed electrode shown in Fig. 10a, have been printed using the method described in Fig. 2, with horizontally deposited ink strips with small spaces in between each deposition of electrode slurry, the gap allows for ink slumping. The resulting pattern width was an electrode with horizontal stripes of graphite with a width of ~ 1.09 (7) mm, (measured using ImageJ software), and gap of 0.050(3) mm, as observed from the top of the electrode. The channels between the printed shapes, presented in Fig. 10b, has a trapezoidal shape, and was measured using an optical microscope (Figs. S5 and S6) with mean length measured from the bottom of the current collector, was established to be 0.020(4) mm, see Fig. 11. The thickness of the electrode was between 145 and 170 μm.

4. Electrochemical testing and transport parameters

The formation cycles, cycle life and electronic and ionic transport parameters were investigated through galvanostatic charge discharge, GITT and EIS measurements. Fig. 12 compares the first lithiation and delithiation cycles of the graphite half-cells from draw down coatings without additive, and with 1.0 wt% 1-octanol as well as the printed electrode with octanol modified ink. The results demonstrate comparable first cycle behaviour of the printed electrode in comparison to the draw-down anodes. The printed electrode exhibited a reversible capacity of 339.4 mA.h g^{-1} with a coulombic efficiency of 80%, which is likely due to improved wetting of the thick printed electrodes compared to the draw down electrodes.

To compare the electrochemical performance of these high coat weight and thick printed and doctor blade coated electrode, the cells underwent galvanostatic charge and discharge cycling with impedance testing after formation and cycling, to note the change in the charge transfer resistances. The rate in change of capacity was measured by comparing the lithiation capacity of the 50th cycle with the 5th. The spread in the data also shows the reproducibility of the electrochemical testing and indicates a degree of inhomogeneity in some of the electrode coatings. (Fig. 13). Significantly lower capacity fade was observed for the cells made from the printed electrodes.

The electrochemical reaction kinetics for the anode half cells was measured by PEIS before and after cycling. The Table 3 shows the data obtained from the fitted PEIS spectra with the equivalent circuit model, Fig. 14.

Fig. 14 compares the Nyquist plot of the impedance for a 1% octanol content slurry for the doctor blade and printed electrodes. A full summary of the different octanol content and doctor blade coated electrodes is provided in Supplementary data Fig. S3. The

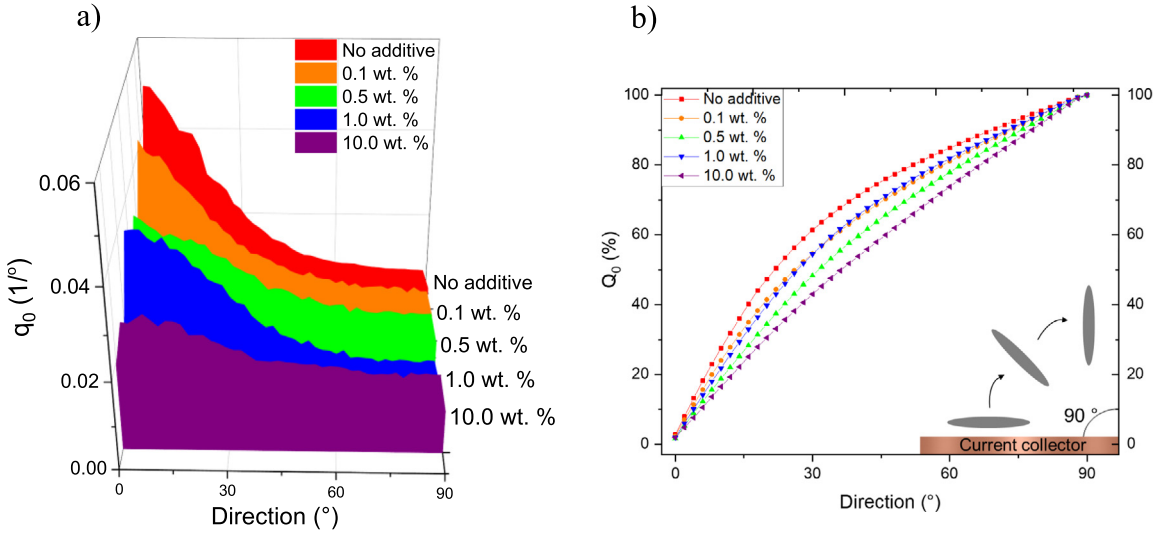

Fig. 7. Differential distribution (a), and the cumulative distribution (b) of the of the graphite particle orientation relative to the current collector, comparing all the investigated electrodes from the tape cast coating.

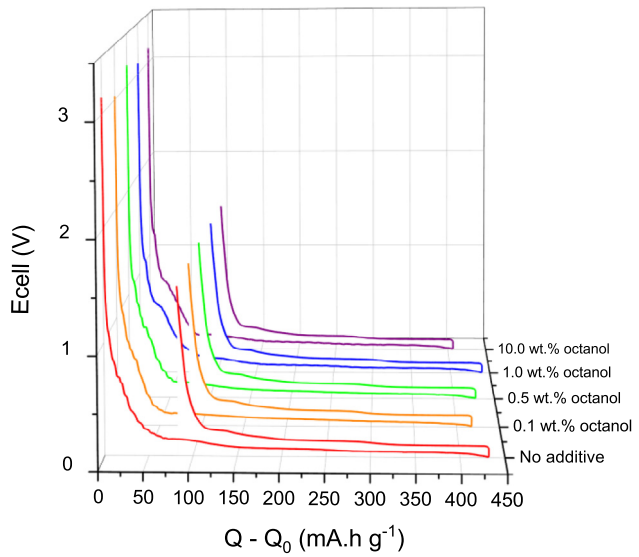

Fig. 8. First lithiation and delithiation cycle for the graphite vs lithium cells with increasing octanol concentrations.

Table 2
Gravimetric capacities for the half-cells containing different concentrations of the secondary fluid with corresponding efficiencies values for the first cycles.

Additive content	Gravimetric capacity (mA.h g^{-1})	Efficiency (%)
No additive	349.4	80.8
0.1 wt%	332.6	79.6
0.5 wt%	340.1	79.6
1.0 wt%	347.9	79.0
10.0 wt%	310.3	76.3

contribution to the observed impedance can be deconvoluted as discussed in the experimental section. The minor differences between each series resistance can be attributed to the porosity and the degree of dispersion of the conductive additive throughout the graphite electrode. The draw-down electrodes gave series resistances of ~ 3 Ω whereas the printed electrode gave an increased series resistance of 4.6 Ω. This is expected as, in-order to maintain the same coat-weight between each electrode, the printed electrodes contain thicker strips of graphite electrode, sandwiched between the electrolyte channels. The structure results in higher ionic resistance due to the thickness of the electrode, and with the additional electrolyte channels, a greater quantity of electrolyte is required to fill all the pore spaces. The total charge transfer can be attributed to the impedances observed between about 10hz and 100 kHz, above 100 kHz the contact resistance R_{con} can be observed as a small semi-circle in the Nyquist plot above ~ 100 kHz and is between 0.2 and 0.8 Ω for all electrodes, with the largest contact resistance being noted for the 10% octanol addition due to the reduced contact between the graphite and the current collector with the agglomerated particles. The printed electrode also exhibited a slightly higher contact resistance of 0.4 Ω as expected from the reduced contact areas with the electrode coating, and thicker coating.

The charge transfer impedance is a combination of the electronic and ionic transport within the pore network and the graphite. After formation, an impedance contribution from the surface electrolyte interface layer is also likely but cannot be deconvoluted from the other impedances in this case. This may explain why the charge transfer of the 10% octanol additive is lower than the other charge transfer resistances, as the agglomeration of graphite results in lower surface area, and therefore lower SEI resistance contributions. The pore size of the 10% octanol draw-

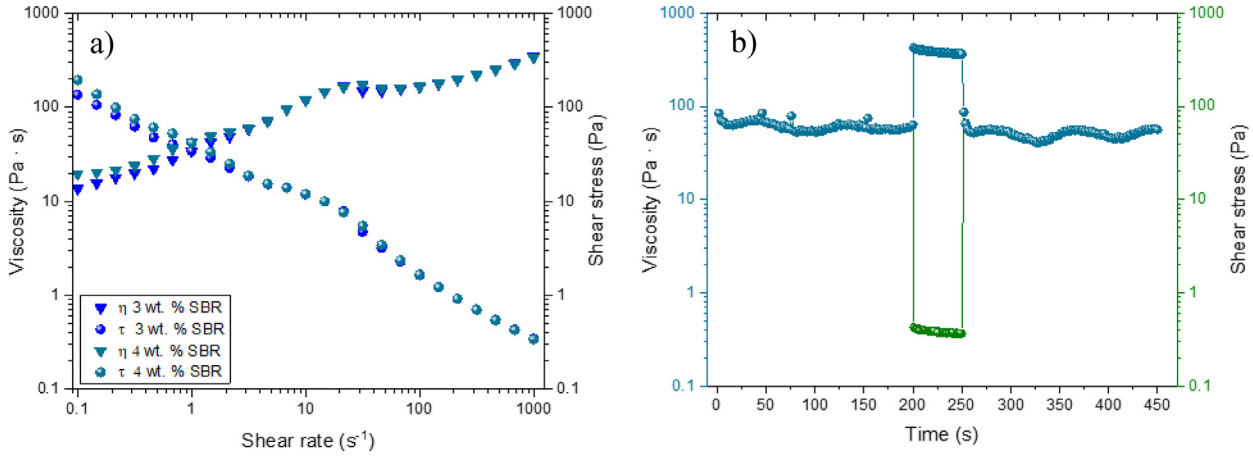

Fig. 9. (a) Flow behaviour curves for the anode inks prepared with an addition of 1.0 wt% of 1-octanol and modified concentration of SBR (b) and 3ITT measurement of the ink applied for the digital printing.

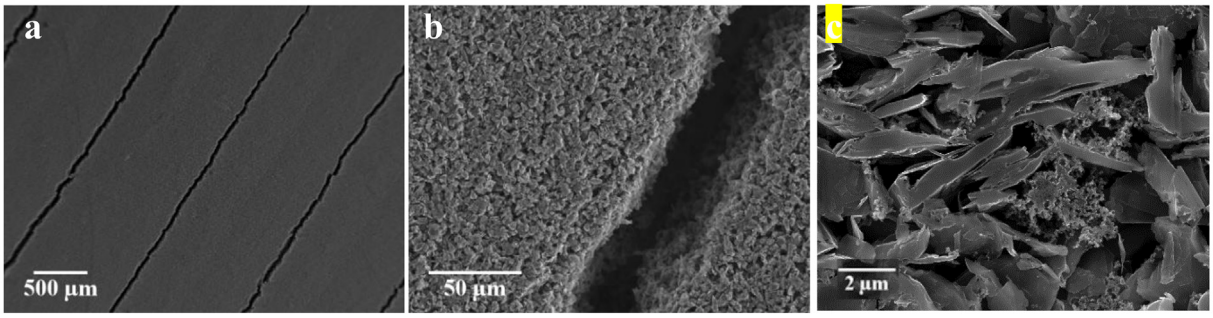

Fig. 10. SEM micrographs of the strips of graphite electrodes digitally printed, from a slurry containing 1.0 wt% 1-octanol (a) showing the active electrode strips and the electrolyte channels at a macro scale and (b) mesoscale. (c) Cross-sectional SEM image of the graphite deposits showing the tortuosity and alignment of the graphite particles.

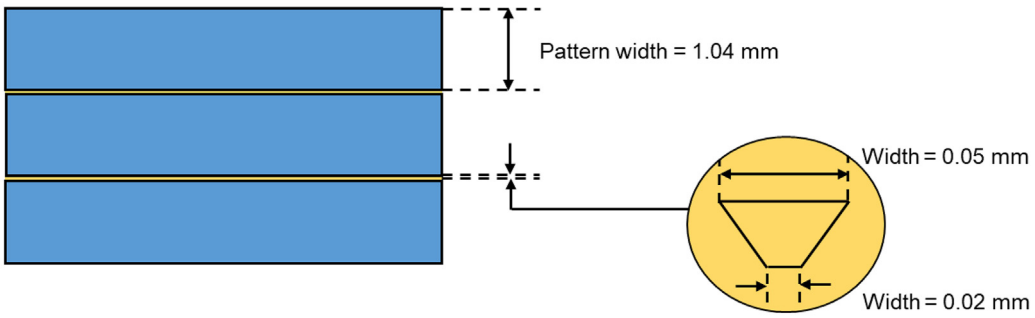

Fig. 11. Schematic illustration of the syringe deposited electrode, with a 1.04 m strip of electrode, and a corresponding 0.05 mm gap between deposition strips. The electrode 'stripe' was trapezoidal in shape with a wider gap at the top (0.05 mm) compared to the bottom at the current collector of (0.02 mm).

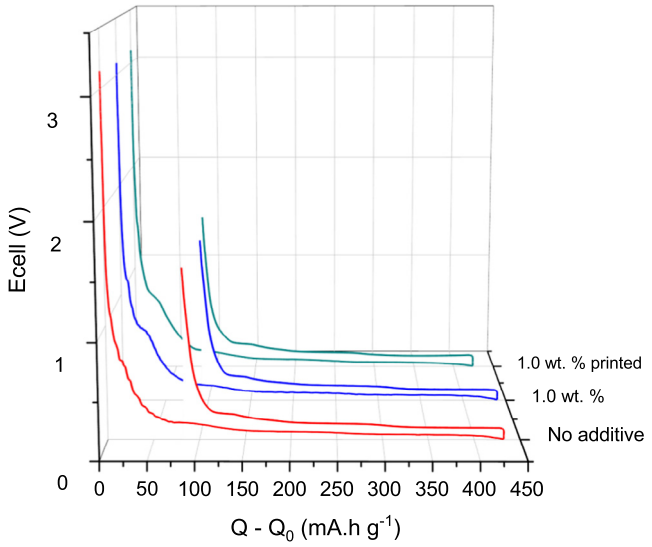

Fig. 12. Comparison of the formation cycles with no viscosity modification and with 1.0 wt% 1-octanol content for both drawdown coating and digitally printed electrodes.

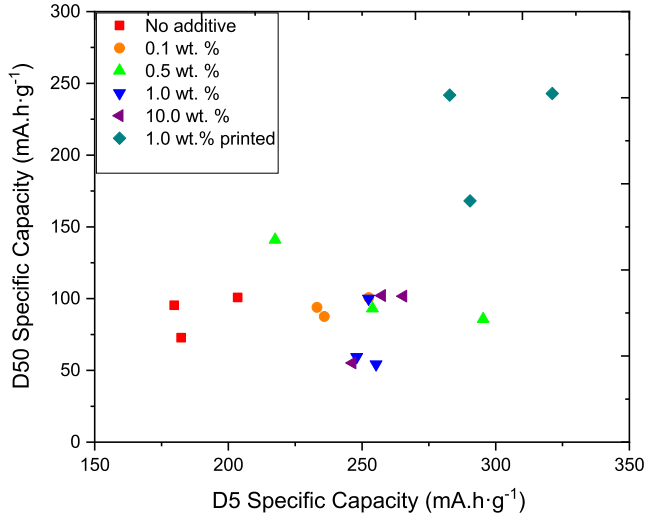

Fig. 13. Capacity fade from the D5 and D50 cycles (lithiation), and the spread in the observed electrochemical data from the drawdown coating containing different concentration of the 1-octanol and the digitally printed electrodes comprising 1.0 wt% of the viscosity modifier.

down coating is also much larger, which reduces the R_{ion} contributions from the electrolyte. For the 1 wt% octanol printed electrolyte, there are two competing R_{ion} contributions, the increased interconnected pore network resistance (or higher tortuosity) from the thicker printed graphite stripes, and the low tortuosity contribution to R_{ion} from the electrolyte channel. However, as observed from the increase in the charge transfer resistance, it is likely that due to the width of the stripes the electrolyte channel does not have a significant impact upon improving the ionic transport mechanisms, in this case, and the increased charge transfer is from the additional electronic and ionic resistances from the thicker electrodes. These results indicate that the electrode design features can be further optimised by changing the ratios and sizes of the channel to the active strip.

For the cycled electrodes there are two distinctive larger semicircles between the frequencies 10 Hz – 100 kHz. The higher frequency impedance likely from the contribution of the increase in SEI impedance upon cycling, whereas the lower impedance is likely from the charge transfer and pore resistance of the electrode. It is observed that the total impedance from the SEI and the charge transfer is significantly lower in the printed electrode after cycling than in the draw-down electrodes. R_S is slightly larger than for the formed electrodes, as is expected. The SEI contribution (R_2) was between 8 and 14 Ω, and the assumed charge transfer resistances (R_3) were slightly higher to those observed in the formed electrodes, apart from the printed electrode which exhibited the lowest resistance of 4.3 Ω. We assume that R_3 is related to the charge transfer impedance from the pore network and graphite which reduces as the tortuosity decreases. Tor the printed electrode the tortuosity and R_3 are much lower, indicating that the reduction in the tortuosity from the electrolyte channel has a significant impact upon the transport mechanism in these cycled electrodes. It is likely that increase in the SEI resistance leads to significant transport limitations in these thick electrodes. The electrolyte channel in the printed electrode provides an additional ion transport mechanism and reduces the electrolyte transport distance to the active graphite components. This in turn, reduces the R_{ion} contribution to the resistance which is exhibited through the lower observed R_3 resistances. The diffusion coefficients were measured using GITT for 0% and 1% octanol addition to the slurry (Fig. S6). A summary of the parameters obtained from the electrochemical and image-based analysis are shown in in Table 3.

The patterned electrode demonstrates improved kinetics of Li^+ deintercalation in comparison to the conventional drawdown electrodes, as demonstrated by the slightly higher apparent diffusion coefficient. The micro-size channels between the layers of the active material contribute to the improved ionic transport and prevent resistance growth from the SEI layer which grows upon cycling [52].

In addition, it can be observed from the cycling performance that the cells incorporating octanol-modified electrodes display higher discharge capacities than the electrodes without the secondary fluid. This phenomena can be attributed to the 1-octanol

Table 3
A summary of the resistance, current exchange, diffusion coefficients and the physical tortuosity and McMullan numbers calculated from the equivalent circuit fitting to the PEIS data, and GITT of the graphite-lithium half cells, and the SEM image analysis (a) before cycling and after formation (b) and after cycling,

(a) Parameter/ Sample ID	Unit	No add.	0.1 wt%	0.5 wt%	1.0 wt%	10.0 wt%	1.0 wt% printed
Rs	(Ω)	3.45	2.92	3.18	3.26	3.05	4.57
R_{con}	(Ω)	0.33	0.19	0.21	0.25	0.88	0.41
R_{CT}	(Ω)	7.26	6.95	6.69	6.94	5.92	12.44*
R_3	(Ω)	48.32	52.84	50.16	51.4	59.36	N/A
σ	(S ·cm^{-1})	9.39 ·10^{-4}	9.19 ·10^{-4}	1.19 ·10^{-3}	1.29 ·10^{-3}	1.47 ·10^{-3}	9.39 ·10^{-4}
j_0	(mA cm^{-2})	5.29 ·10^{-2}	5.88 ·10^{-2}	5.99 ·10^{-2}	5.82 ·10^{-2}	6.70 ·10^{-2}	5.96 ·10^{-5}
D_{Li} (GITT)	(cm^2 s^{-1})	9.82 ·10^{-11}	–	–	1.06 ·10^{-10}	–	1.58 ·10^{-10}
τ through plane	–	5.3(1)	4.6(4)	3.5(3)	3.4(1)	2.8(4)	3.9(3) / 1
τ in plane	–	2.5(1)	2.4(1)	2.3(1)	2.1(1)	2.1(2)	2.3(2)
N_M	–	8.93	7.66	5.21	4.78	4.01	5.41 / 1
(b) Parameter/ Sample ID	**Unit**	**No add.**	**0.1 wt%**	**0.5 wt%**	**1.0 wt%**	**10.0 wt%**	**1.0 wt% printed**
Rs	(Ω)	3.49	7.43	4.39	6.87	5.77	7.81
R_{SEI}	(Ω)	9.18	14.46	11.19	13.29	13.61	13.26
R_3	(Ω)	10.14	8.71	6.12	8.83	6.51	4.29
σ	(S ·cm^{-1})	6.59 · 10^{-4}	7.33 · 10^{-4}	1.30 · 10^{-3}	1.02 · 10^{-3}	1.34 · 10^{-3}	2.72 · 10^{-3}
j_0	(mA cm^{-2})	3.79 ·10^{-2}	4.69 ·10^{-2}	6.55 ·10^{-2}	4.57 ·10^{-2}	6.09 ·10^{-2}	1.73 ·10^{-1}

* The PEIS of the printed electrode showed an combined frequency response to the R_{ion} and the R_{CT} compared to the tape cast coatings, and no R_3 was observed.

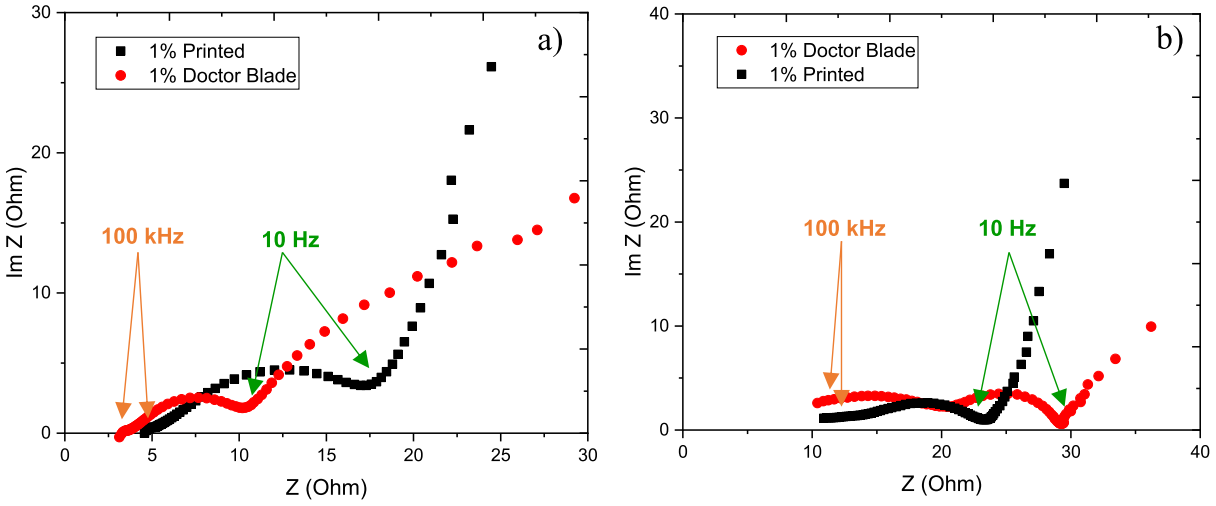

Fig. 14. Nyquist plots (a) the magnification of the high frequency region (1 Hz–500 kHz) for the cells after formation cycle (a) and after cycling (10 mHz–500 kHz) (b) for 1% octanol in the slurry composition for the Dr Blade (Red) vs Printed (black) coated electrodes, respectively. (For interpretation of the references to colour in this figure legend, the reader is referred to the web version of this article.)

containing electrodes exhibiting improved CB percolation and higher porosities which contributes to the improved lithium-ion diffusion, combined with a faster electron transport at the same time explained by the short-range electrical contacts [53]. Moreover, it should be noted that the alignment of the graphite particles in the electrodes has an influence on the ionic and electronic conductivity [54,55]. It is known that a resistivity of graphite in c-axis direction is 10^{-2} Ω·cm, whereas, in the a-axis direction is 4×10^{-5} Ω·cm. The lithium intercalation into graphite occurs along the a-axis – perpendicular to the direction of the current flow [36]. It was observed on the SEM micrographs, Fig. 5, that the alignment of the graphite particles in the electrodes containing 0.5 wt% and 1.0 wt% of 1-octanol has become more perpendicular to the current collector (c-axis parallel). The MacMullin number was shown to decrease with increasing octanol content and the tortuosity decreased. The printed electrode is more difficult to assess as the electrolyte channels would have a tortuosity of 1, whereas the coated parts of the electrodes exhibited a tortuosity of around 3.93. However, it can be observed that the alignment of the graphite to the current collector in the printed electrode is comparable to the 10% octanol, but the particles are not agglomerated, and the carbon black is well dispersed as shown in Fig. 10, Table S1 and Fig. S2. The conductivities and exchange currents of the electrodes also increase with increasing octanol content and is highest for the printed electrodes as shown from the PEIS analysis of the cycled electrodes. Due to the merging of the respective observed frequency responses in the formed electrodes, the comparison of the conductivities of the draw-down and printed electrodes is more difficult. However, the electrodes which exhibited highest electronic conductivities in conjunction with a lower tortuosity also showed higher diffusion coefficients. This indicates that improved lifetime can be achieved through microstructure control to improve electronic conductivity and reduce tortuosity. Further improvements in electronic conductivity of the coatings can be achieved through calendaring and formulation changes. However, this may change the carefully controlled microstructure of the electrodes and the alignment of the graphite particles and needs further investigation.

5. Conclusions

This work illustrates the importance of microstructure design upon the performance properties of lithium-ion battery electrodes.

The internal pore and electronic networks for electronic and ionic transport can be manipulated through rheological changes in the inks and through deposition method. A flake graphite model system is demonstrated with a small particle size graphite (KS6) as an example lithium-ion anode material. This material can be utilised in conjunction with the printing dispenser and does not block the printing nozzle. The inks were optimised through the addition of a secondary solvent, 1-octanol. The rheological properties of the inks were modified successfully for both tape casting and digital syringe deposition printing methods of high coat weight graphite battery electrodes. The addition of the secondary solvent (0% to 10% 1-octanol) in water provided design changes in the microstructures of the as made electrodes, for both the pore-network and tortuosity, carbon black distribution and the flake graphite alignment. With more octanol less alignment of the particles to the current collector was observed and improved distribution of the carbon black throughout the electrode. At 10% octanol the particles agglomerated, and the microstructure of the electrodes collapsed. The syringe deposited electrode with 1% octanol secondary solvent produced an electrode which exhibited a tortuosity similar to that of the tape cast electrode (3.9 *cf* 3.4), and the additional electrolyte channel designed into the electrode provided enhanced ion transport. These electrodes exhibited improved life-time properties because of the optimised ion transport network. The improved cycle life can be related not only to the improved lithium-ion transport properties through the channels in the electrode, but the greater dispersion of the carbon black, even though the electrode strips exhibited higher tortuosity compared to the draw-down electrodes. The extrapolated resistances from the impedance spectroscopy showed that with higher octanol content greater electronic conductivities were observed. The electrodes with lower tortuosity and high electronic conductivity exhibited higher observed diffusion coefficients. The structured electrode manufactured through syringe extrusion deposition showed highest conductivities, lowest average tortuosity, less alignment of the graphite to the current collector, higher diffusion coefficients and longer cycle life. Further work is still required to further optimise inks with battery electrodes; however, this shows the initial steps required in printing optimisation and opens up many further avenues of design and control of electrode microstructures to optimise performance properties.

CRediT authorship contribution statement

Dominika Gastol: Methodology, Formal analysis, Investigation, Writing - original draft, Writing - review & editing. **Matthew Capener:** Methodology, Investigation, Writing - review & editing. **Carl Reynolds:** Formal analysis, Writing - review & editing. **Christopher Constable:** Formal analysis, Writing - review & editing. **Emma Kendrick:** Conceptualization, Formal analysis, Writing - original draft, Writing - review & editing, Supervision, Funding acquisition.

Declaration of Competing Interest

The authors declare that they have no known competing financial interests or personal relationships that could have appeared to influence the work reported in this paper.

Acknowledgements

Authors would like to acknowledge Innovate UK Spraycoat Project 133364, and KWSP who designed and manufactured the digital deposition equipment. Also, Faraday Institution project (faraday.ac.uk; EP/S003053/1, FIRG015).

Appendix A. Supplementary material

Supplementary data to this article can be found online at https://doi.org/10.1016/j.matdes.2021.109720.

References

[1] X. Wu, S. Xia, Y. Huang, X. Hu, B. Yuan, S. Chen, Y. Yu, W. Liu, High-performance, low-cost, and dense-structure electrodes with high mass loading for lithium-ion batteries, Adv. Funct. Mater. 29 (2019) 1903961, https://doi.org/10.1002/adfm.201903961.
[2] As battery costs plummet, lithium-ion innovation hits limits, experts say | S&P Global Market Intelligence, (n.d.). https://www.spglobal.com/marketintelligence/en/news-insights/latest-news-headlines/as-battery-costs-plummet-lithium-ion-innovation-hits-limits-experts-say-58613238 (accessed October 12, 2020).
[3] J. Schnell, G. Reinhart, Quality management for battery production: a quality gate concept, Procedia CIRP, Elsevier B.V. (2016) 568–573, https://doi.org/10.1016/j.procir.2016.11.098.
[4] X. Gao, X. Liu, R. He, M. Wang, W. Xie, N.P. Brandon, B. Wu, H. Ling, S. Yang, Designed high-performance lithium-ion battery electrodes using a novel hybrid model-data driven approach, Energy Storage Mater. 36 (2021) 435–458, https://doi.org/10.1016/j.ensm.2021.01.007.
[5] K. Song, C. Zhang, N. Hu, X. Wu, L. Zhang, High performance thick cathodes enabled by gradient porosity, Electrochim. Acta. 377 (2021), https://doi.org/10.1016/j.electacta.2021.138105 138105.
[6] M. Singh, J. Kaiser, H. Hahn, Thick electrodes for high energy lithium ion batteries, J. Electrochem. Soc. 162 (2015) A1196–A1201, https://doi.org/10.1149/2.0401507jes.
[7] J. Li, Z. Du, R.E. Ruther, S.J. An, L.A. David, K. Hays, M. Wood, N.D. Phillip, Y. Sheng, C. Mao, S. Kalnaus, C. Daniel, D.L. Wood, Toward low-cost, high-energy density, and high-power density lithium-ion batteries, Jom. 69 (2017) 1484–1496, https://doi.org/10.1007/s11837-017-2404-9.
[8] Y. Kuang, C. Chen, D. Kirsch, L. Hu, Thick electrode batteries: principles, opportunities, and challenges, Adv. Energy Mater. 9 (2019) 1–19, https://doi.org/10.1002/aenm.201901457.
[9] Z. Guo, H. Yao, Thickness gradient promotes the performance of Si-based anode material for lithium-ion battery, Mater. Des. 195 (2020), https://doi.org/10.1016/j.matdes.2020.108993 108993.
[10] Y.C. Lu, B.M. Gallant, D.G. Kwabi, J.R. Harding, R.R. Mitchell, M.S. Whittingham, Y. Shao-Horn, Lithium-oxygen batteries: Bridging mechanistic understanding and battery performance, Energy Environ. Sci. 6 (2013) 750–768, https://doi.org/10.1039/c3ee23966g.
[11] Lithium Sulphur Battery Advantages And Disadvantages-battery-knowledge | Large Power, (n.d.). https://www.large.net/news/8eu43mx.html (accessed November 11, 2020).
[12] B. Liu, Y. Sun, L. Liu, J. Chen, B. Yang, S. Xu, X. Yan, Recent advances in understanding Li-CO2 electrochemistry, Energy Environ. Sci. 12 (2019) 887–922, https://doi.org/10.1039/c8ee03417f.
[13] S. Nanda, A. Manthiram, Lithium degradation in lithium-sulfur batteries: Insights into inventory depletion and interphasial evolution with cycling, Energy Environ. Sci. 13 (2020) 2501–2514, https://doi.org/10.1039/d0ee01074j.
[14] E. Kendrick, Chapter 11: Advancements in manufacturing, in: RSC Catal. Ser., Royal Society of Chemistry, 2019: pp. 262–289. Doi: 10.1039/9781788016124-00262.
[15] T.S. Wei, B.Y. Ahn, J. Grotto, J.A. Lewis, 3D printing of customized li-ion batteries with thick electrodes, Adv. Mater. 30 (2018), https://doi.org/10.1002/adma.201703027.
[16] C. Huang, N.P. Young, J. Zhang, H.J. Snaith, P.S. Grant, A two layer electrode structure for improved Li Ion diffusion and volumetric capacity in Li Ion batteries, Nano Energy 31 (2017) 377–385, https://doi.org/10.1016/j.nanoen.2016.11.043.
[17] W. Lai, C.K. Erdonmez, T.F. Marinis, C.K. Bjune, N.J. Dudney, F. Xu, R. Wartena, Y.M. Chiang, Ultrahigh-energy-density microbatteries enabled by new electrode architecture and micropackaging design, Adv. Mater. 22 (2010), https://doi.org/10.1002/adma.200903650.
[18] A.M. Gaikwad, A.C. Arias, D.A. Steingart, Recent progress on printed flexible batteries: mechanical challenges, printing technologies, and future prospects, Energy Technol. 3 (2014) 305–328, https://doi.org/10.1002/ente.201402182.
[19] A. Izumi, M. Sanada, K. Furuichi, K. Teraki, T. Matsuda, K. Hiramatsu, H. Munakata, K. Kanamura, Development of high capacity lithium-ion battery applying three-dimensionally patterned electrode, Electrochim. Acta. 79 (2012) 218–222, https://doi.org/10.1016/j.electacta.2012.07.001.
[20] K. Evanoff, J. Khan, A.A. Balandin, A. Magasinski, W.J. Ready, T.F. Fuller, G. Yushin, Towards ultrathick battery electrodes: Aligned carbon nanotube-enabled architecture, Adv. Mater. 24 (2012) 533–537, https://doi.org/10.1002/adma.201103044.
[21] X. Lu, S.R. Daemi, A. Bertei, M.D.R. Kok, K.B. O'Regan, L. Rasha, J. Park, G. Hinds, E. Kendrick, D.J.L. Brett, P.R. Shearing, Microstructural evolution of battery electrodes during calendering, Joule (2020), https://doi.org/10.1016/j.joule.2020.10.010.
[22] C.-H. Chen, F. Brosa Planella, K. O'Regan, D. Gastol, W.D. Widanage, E. Kendrick, Development of experimental techniques for parameterization of multi-scale

lithium-ion battery models, J. Electrochem. Soc. 167 (2020), https://doi.org/10.1149/1945-7111/ab9050 080534.
[23] Z. Du, D.L. Wood, C. Daniel, S. Kalnaus, J. Li, Understanding limiting factors in thick electrode performance as applied to high energy density Li-ion batteries, J. Appl. Electrochem. 47 (2017) 405–415, https://doi.org/10.1007/s10800-017-1047-4.
[24] V. Srinivasan, J. Newman, Design and optimization of a natural graphite/iron phosphate lithium-ion cell, J. Electrochem. Soc. 151 (2004) A1530, https://doi.org/10.1149/1.1785013.
[25] D. Dang, Y. Wang, S. Gao, Y.T. Cheng, Freeze-dried low-tortuous graphite electrodes with enhanced capacity utilization and rate capability, Carbon N. Y. 159 (2020) 133–139, https://doi.org/10.1016/j.carbon.2019.12.036.
[26] B. Bitsch, J. Dittmann, M. Schmitt, P. Scharfer, W. Schabel, N. Willenbacher, A novel slurry concept for the fabrication of lithium-ion battery electrodes with beneficial properties, J. Power Sources. 265 (2014) 81–90, https://doi.org/10.1016/j.jpowsour.2014.04.115.
[27] M. Schneider, E. Koos, N. Willenbacher, Highly conductive, printable pastes from capillary suspensions, Sci. Rep. 6 (2016) 1–10, https://doi.org/10.1038/srep31367.
[28] E. Koos, N. Willenbacher, Capillary forces in suspension rheology, Science (80-.). 331 (2011) 897–900. Doi: 10.1126/science.1199243.
[29] E. Koos, Europe PMC Funders Group Capillary suspensions : Particle networks formed through the capillary force, 19 (2015) 575–584. Doi: 10.1016/j.cocis.2014.10.004.Capillary.
[30] B. Bitsch, B. Braunschweig, N. Willenbacher, Interaction between polymeric additives and secondary fluids in capillary suspensions, Langmuir 32 (2016) 1440–1449, https://doi.org/10.1021/acs.langmuir.5b03861.
[31] B. Bitsch, T. Gallasch, M. Schroeder, M. Börner, M. Winter, N. Willenbacher, Capillary suspensions as beneficial formulation concept for high energy density Li-ion battery electrodes, J. Power Sources. 328 (2016) 114–123, https://doi.org/10.1016/j.jpowsour.2016.07.102.
[32] M. Schneider, J. Maurath, S.B. Fischer, M. Weiß, N. Willenbacher, E. Koos, Suppressing crack formation in particulate systems by utilizing capillary forces, ACS Appl. Mater. Interfaces. 9 (2017) 11095–11105, https://doi.org/10.1021/acsami.6b13624.
[33] Innovate UK Spraycoat Project 133364, n.d.
[34] H.K.D.H. Bhadeshia, Additive manufacturing, Mater. Sci. Technol. (United Kingdom) 32 (2016) 615–616, https://doi.org/10.1080/02670836.2016.1197523.
[35] K.B. Singh, M.S. Tirumkudulu, Cracking in drying colloidal films, Phys. Rev. Lett. 98 (2007) 1–4, https://doi.org/10.1103/PhysRevLett.98.218302.
[36] J.Y. Kim, K. Cho, S.A. Ryu, S.Y. Kim, B.M. Weon, Crack formation and prevention in colloidal drops, Sci. Rep. 5 (2015) 1–9, https://doi.org/10.1038/srep13166.
[37] GV Series Automated Dispensing Systems, Operating Manual for Gantry Robots. Nordson EFD manuals, www.nordsonefd.com, (n.d.).
[38] S.J. An, J. Li, Z. Du, C. Daniel, D.L. Wood, Fast formation cycling for lithium ion batteries, J. Power Sources. 342 (2017) 846–852, https://doi.org/10.1016/j.jpowsour.2017.01.011.
[39] D. Aurbach, B. Markovsky, I. Weissman, E. Levi, Y. Ein-Eli, On the correlation between surface chemistry and performance of graphite negative electrodes for Li ion batteries, Electrochim. Acta. 45 (1999) 67–86, https://doi.org/10.1016/S0013-4686(99)00194-2.
[40] T.S. Pathan, M. Rashid, M. Walker, W.D. Widanage, E. Kendrick, Active formation of Li-ion batteries and its effect on cycle life, J. Phys. Energy. 1 (2019), https://doi.org/10.1088/2515-7655/ab2e92 044003.
[41] N. Meddings, M. Heinrich, F. Overney, J.S. Lee, V. Ruiz, E. Napolitano, S. Seitz, G. Hinds, R. Raccichini, M. Gaberšček, J. Park, Application of electrochemical impedance spectroscopy to commercial Li-ion cells: A review, J. Power Sources. 480 (2020), https://doi.org/10.1016/j.jpowsour.2020.228742 228742.
[42] A. Nyman, M. Behm, G. Lindbergh, Electrochemical characterisation and modelling of the mass transport phenomena in LiPF6-EC-EMC electrolyte, Electrochim. Acta. 53 (2008) 6356–6365, https://doi.org/10.1016/j.electacta.2008.04.023.
[43] J. Huang, Z. Li, J. Zhang, S. Song, Z. Lou, N. Wu, An analytical three-scale impedance model for porous electrode with agglomerates in lithium-ion batteries, J. Electrochem. Soc. 162 (2015) A585–A595, https://doi.org/10.1149/2.0241504jes.
[44] S.J. Cooper, A. Bertei, P.R. Shearing, J.A. Kilner, N.P. Brandon, TauFactor: An open-source application for calculating tortuosity factors from tomographic data, SoftwareX. 5 (2016) 203–210, https://doi.org/10.1016/j.softx.2016.09.002.
[45] J. Landesfeind, J. Hattendorff, A. Ehrl, W.A. Wall, H.A. Gasteiger, Tortuosity determination of battery electrodes and separators by impedance spectroscopy, J. Electrochem. Soc. 163 (2016) A1373–A1387, https://doi.org/10.1149/2.1141607jes.
[46] M.R. Somalu, A. Muchtar, W.R.W. Daud, N.P. Brandon, Screen-printing inks for the fabrication of solid oxide fuel cell films: A review, Renew. Sustain. Energy Rev. 75 (2017) 426–439, https://doi.org/10.1016/j.rser.2016.11.008.
[47] S. Bindgen, F. Bossler, J. Allard, E. Koos, Connecting particle clustering and rheology in attractive particle networks, Soft Matter 16 (2020) 8380–8393, https://doi.org/10.1039/d0sm00861c.
[48] M. Youssry, D. Guyomard, B. Lestriez, Carbon black dispersions in surfactant-based microemulsion, J. Mater. Res. 33 (2018) 1301–1307, https://doi.org/10.1557/jmr.2017.451.
[49] Q. Yuan, D. Wu, Low percolation threshold and high conductivity in carbon black filled polyethylene and polypropylene composites, J. Appl. Polym. Sci. 115 (2010) 3527–3534, https://doi.org/10.1002/app.30919.
[50] K. Zaghib, G. Nadeau, K. Kinoshita, Effect of graphite particle size on irreversible capacity loss, J. Electrochem. Soc. 147 (2000) 2110, https://doi.org/10.1149/1.1393493.
[51] S.J. An, J. Li, C. Daniel, D. Mohanty, S. Nagpure, D.L. Wood, The state of understanding of the lithium-ion-battery graphite solid electrolyte interphase (SEI) and its relationship to formation cycling, Carbon N. Y. 105 (2016) 52–76, https://doi.org/10.1016/j.carbon.2016.04.008.
[52] J. Li, M.C. Leu, R. Panat, J. Park, A hybrid three-dimensionally structured electrode for lithium-ion batteries via 3D printing, Mater. Des. 119 (2017) 417–424, https://doi.org/10.1016/j.matdes.2017.01.088.
[53] H. Bockholt, W. Haselrieder, A. Kwade, Intensive powder mixing for dry dispersing of carbon black and its relevance for lithium-ion battery cathodes, Powder Technol. 297 (2016) 266–274, https://doi.org/10.1016/j.powtec.2016.04.011.
[54] Z.X. Shu, R.S. McMillan, J.J. Murray, Electrochemical intercalation of lithium into graphite, J. Electrochem. Soc. 140 (1993) 922–927, https://doi.org/10.1149/1.2056228.
[55] G. Inoue, M. Kawase, Numerical and experimental evaluation of the relationship between porous electrode structure and effective conductivity of ions and electrons in lithium-ion batteries, J. Power Sources. 342 (2017) 476–488, https://doi.org/10.1016/j.jpowsour.2016.12.098.